The Modelling of an SF_6 Arc in a Supersonic Nozzle: II. Current Zero Behaviour of the Nozzle Arc

Q Zhang, J Liu, J D Yan and M T C Fang
Department of Electrical Engineering and Electronics, University of Liverpool, Brownlow Hill, Liverpool L69 3GJ, UK

Email: zhangq12@liverpool.ac.uk, ee0u927d@liverpool.ac.uk, yaneee@liverpool.ac.uk and ee24@liverpool.ac.uk

Abstract. The present work (Part II) forms the second part of an investigation into the behaviour of SF_6 nozzle arc. It is concerned with the aerodynamic and electrical behaviour of a transient nozzle arc under a current ramp specified by a rate of current decay (di/dt) before current zero and a voltage ramp (dV/dt) after current zero. The five flow models used in Part I [1] for cold gas flow and DC nozzle arcs have been applied to study the transient arc at three stagnation pressures (P_0) and two values of di/dt for the current ramp, representing a wide range of arcing conditions. An analysis of the physical mechanisms encompassed in each flow model is given with an emphasis on the adequacy of a particular model in describing the rapidly varying arc around current zero. The critical rate of rise of recovery voltage (RRRV) is found computationally and compared with test results of Benenson et al [2]. For transient nozzle arcs, the RRRV is proportional to the square of P_0, rather than to the square root of P_0 for DC nozzle arcs. The physical mechanisms responsible for the strong dependence of RRRV on P_0 have been investigated. The relative merits of the flow models employed are discussed.

1 Introduction

There is now consensus that an SF_6 arc in the nozzle interrupter of a high voltage circuit breaker is turbulent [1, 3-6]. Modelling of turbulent arcs is still in its infancy as the mechanisms for generating arc instability and maintaining turbulence in the arc context are little understood. However, there is a direct resemblance between a high velocity free jet in a stagnant external flow and an arc surrounded by a cold and low speed flow in a nozzle, both of which are dominated by shear flow. Therefore, the approach of the first choice for turbulent arc modelling at present is to apply those turbulence models that have been used successfully for the modelling of turbulent shear flows. Up until now, the commonly used models for turbulent nozzle arcs have been based on the concept of eddy viscosity [7]. Of these turbulence models, the Prandtl mixing length model has achieved considerable success in predicting turbulent SF_6 arc behaviour [8-11]. Modelling of turbulent arc and turbulent flow in circuit breakers based on the

standard k-epsilon model [9, 12] and its variants (e.g. the RNG model [6], the Chen-Kim model [13] and the realizable model [6, 14]), yields conflicting claims regarding the success of these models. The test conditions in terms of current, pressure and system geometry covered by the aforementioned investigations are very limited, and thus no general conclusions can be drawn on the relative merits of the turbulence models so far employed. This has prompted the current investigation into the turbulent behaviour of SF_6 nozzle arcs.

The verification of turbulence models suitable for switching applications requires extensive reproducible experimental results covering a wide range of test conditions. In a circuit breaker, the arc in the nozzle interrupter is often subjected to pressure waves generated in other parts of the breaker due to the interaction between the nozzle interrupter and the rest of the breaker. Under such circumstances, it is difficult to separate the turbulent effects from those due to the aforementioned interaction. To avoid such complication and to focus our attention on the modelling of turbulent effects, we study the nozzle arc in a two-pressure system used by Benenson et al [2]. Experimentally measured critical rate of rise of recovery voltage (RRRV) under a wide range of discharge conditions as reported in [2] will be used to verify and to assess the relative merits of the turbulence models used in current investigation.

In Part I [1] of our investigation, the features of the cold flow and the behaviour of SF_6 DC nozzle arcs are computationally investigated for the nozzle used in [2]. Altogether five flow models, i.e. the laminar flow model, the Prandtl mixing length model, the standard k-epsilon model and its two variants, the Chen-Kim model and the RNG model, have been used. However, no experimentally measured DC arc voltages for the nozzle used in [2] are available for direct comparison with the computational results in Part I. Thus, the relative merits of turbulence models applied cannot be judged. With the available experimental RRRV results [2], we are now in a position to rigorously study and assess the applicability of the flow models for transient nozzle arcs. The present investigation (Part II) is concerned with the aerodynamic and electrical behaviour of the transient nozzle arc under a current ramp specified by a rate of current decay (di/dt) before current zero and a voltage ramp (dV/dt) after current zero. The five flow models, used in Part I [1], will again be used to study the arc behaviour under the discharge conditions specified in [2]. The RRRV of the nozzle used in [2] after current zero will be computed using the five flow models. The computed RRRV will be compared with the measurements reported in [2] at three stagnation pressures, P_0 (11.2 atm, 21.4 atm and 35 atm), and two values of di/dt (13 $A\mu s^{-1}$ and $25 A\mu s^{-1}$) for the current ramp. Based on this comparison, the relative merits of the five flow models will be discussed.

The paper is organized as follows. Section 2 gives a brief description on the governing equations of the turbulent nozzle arc and those of the turbulence models applied. Discussion of the computational results and comparison with experiments are given in Section 3. An analysis of the physical mechanisms encompassed in each flow model will be given to show the adequacy of a particular turbulence model in describing the rapidly varying arc during current zero period. Section 4 presents an investigation on the physical mechanisms responsible for the dependence of RRRV on P_0 as indicated by the experimental results. In Section 5, relative merits of the flow models employed are discussed. Finally, appropriate conclusions are drawn.

2 The governing equations and turbulence models

The governing equations for the nozzle arc together with the reasons for choosing the four aforementioned turbulence models for nozzle arcs are given in Part I [1]. For completeness and easy reference, the governing equations in cylindrical coordinates for an arc in local thermal equilibrium (LTE) are given below:

$$\frac{\partial(\rho\phi)}{\partial t}+\frac{1}{r}\frac{\partial}{\partial r}\left[r\rho v\phi-r\Gamma_\phi\frac{\partial\phi}{\partial r}\right]+\frac{\partial}{\partial z}\left[\rho w\phi-\Gamma_\phi\frac{\partial\phi}{\partial z}\right]=S_\phi \tag{1}$$

where ρ is the gas density and ϕ the dependent variable. When ϕ = 1, equation (1) becomes continuity equation. For ϕ = v (radial velocity) or w (axial velocity) respectively, we obtain radial or axial momentum conservation equation. Energy conservation equation is derived from equation (1) by substituting ϕ with h (enthalpy). The major source term (S_ϕ) for momentum equation is the pressure gradient and those for energy equation are Ohmic heating, σE^2, where electrical field, E, is obtained from the simplified Ohm's law:

$$i = E\int_0^\infty \sigma 2\pi r dr\,, \tag{2}$$

and q the net radiation loss per unit volume and time [1]. In equation (2), integration is up to the nozzle surface (∞). The diffusion coefficients for momentum and energy equations (Γ_ϕ) are given in Part I [1].

The equation of state, the thermodynamic and transport coefficients of SF_6 used in the computations are those tabulated by Frost and Liebermann [15]. For temperature below 1000 K, the equation of state for ideal gas is used. It should be noted that at the highest stagnation pressure investigated, P_0 = 35 atm, there will be departure from state equation of ideal gas for temperature less than 400 K. Such effects have not been considered. For current up to 1 kA, it is sufficiently accurate to calculate electric field using the simplified Ohm's law [1]. The net radiation loss in the energy equation is computed using the approximate model of Zhang et al [16].

By setting the eddy viscosity in the moment equation, μ_t, and turbulent thermal conductivity in the energy equation, k_t, equal to zero, we obtain the laminar flow model. The four turbulence models are those used in Part I [1], i.e. the Prandtl mixing length model, the standard k-epsilon model, the Chen-Kim model and the RNG model. The equations for these turbulence models are given in table 1 for completeness. k_t is related to μ_t through turbulent Prandtl number, Pr_t, which is assumed to be unity [1].

Table 1. A list of the flow models applied in the present investigation.

Flow	Governing equations	Length scale and	Source term (S_ε) and model

<table>
<tr><td>models</td><td></td><td>velocity scale of turbulence and eddy viscosity</td><td>constants</td></tr>
<tr><td>(1) Laminar flow model</td><td>Not applicable</td><td>Not applicable</td><td>Not applicable</td></tr>
<tr><td>(2) Prandtl mixing length model</td><td>Not applicable</td><td>Length scale:
$\lambda_c = cr_\delta$
Velocity scale:
$V_c = \lambda_c\left(\left|\frac{\partial w}{\partial r}\right| + \left|\frac{\partial v}{\partial z}\right|\right)$
Eddy viscosity:
$\mu_t = \rho\lambda_c^2\left(\left|\frac{\partial w}{\partial r}\right| + \left|\frac{\partial v}{\partial z}\right|\right)$
where
$r_\delta = \sqrt{\int_0^\infty\left(1-\frac{T_\infty}{T}\right)2rdr}$</td><td>Not applicable</td></tr>
<tr><td>(3) Standard k-epsilon model</td><td rowspan="3">k-equation:
$\frac{\partial(\rho k)}{\partial t} + \nabla\cdot\left(\rho\vec{V}k - \frac{\rho\nu_t}{\sigma_k}\nabla k\right) = \rho(P_k - \varepsilon)$
Epsilon-equation:
$\frac{\partial(\rho\varepsilon)}{\partial t} + \nabla\cdot\left(\rho\vec{V}\varepsilon - \frac{\rho\nu_t}{\sigma_\varepsilon}\nabla\varepsilon\right) = \rho\frac{\varepsilon}{k}(C_{1e}P_k - C_{2e}\varepsilon) + S_\varepsilon$
where
$P_k = \nu_t\left[2\left(\frac{\partial w}{\partial z}\right)^2 + 2\left(\frac{\partial v}{\partial r}\right)^2 + 2\left(\frac{v}{r}\right)^2 + \left(\frac{\partial w}{\partial r} + \frac{\partial v}{\partial z}\right)^2\right]$</td><td rowspan="3">Length scale:
$\lambda_c \propto k^{1.5}/\varepsilon$
Velocity scale:
$V_c \propto \sqrt{k}$
Eddy viscosity:
$\mu_t = \rho C_\mu k^2/\varepsilon$</td><td>$S_\varepsilon = 0$
$\sigma_k = 1.0$, $\sigma_\varepsilon = 1.3$, $C_{1e} = 1.44$
$C_{2e} = 1.92$, $C_\mu = 0.09$</td></tr>
<tr><td>(4) Chen-Kim k-epsilon model</td><td>$S_\varepsilon = \frac{\rho C_{3e}P_k^2}{k}$
$\sigma_k = 0.75$, $\sigma_\varepsilon = 1.15$,
$C_{1e} = 1.15$, $C_{2e} = 1.90$,
$C_{3e} = 0.25$,$C_\mu = 0.09$</td></tr>
<tr><td>(5) RNG k-epsilon model</td><td>$S_\varepsilon = -\frac{\rho C_\mu\eta^3(1-\eta/\eta_0)}{1+\beta\eta^3}\frac{\varepsilon^2}{k}$
$\eta = (k/\varepsilon)\cdot\sqrt{(\rho P_k/\mu_t)}$,
$\eta_0 = 4.38$, $\beta = 0.012$,
$\sigma_k = \sigma_\varepsilon = 0.7194$,
$C_{1e} = 1.42$, $C_{2e} = 1.68$,
$C_\mu = 0.0845$</td></tr>
</table>

3 Results and discussion

Computation has been performed on the nozzle used by Benenson et al [2]. The nozzle geometry and the distribution of grids for the computation are given in figure 1. Version 3.6.1 of PHOENICS [17] has been used to solve the governing equations. The boundary conditions for the arc conservation equations and those of the k-epsilon model equations are the same as those reported in Part I [1]. At the nozzle inlet, three value of P_0, 11.2 atm, 21.4 atm and 35 atm, have been applied. At the nozzle exit, P_e is set to a very low value to guarantee shock free inside the nozzle in the absence of the downstream electrode [2].

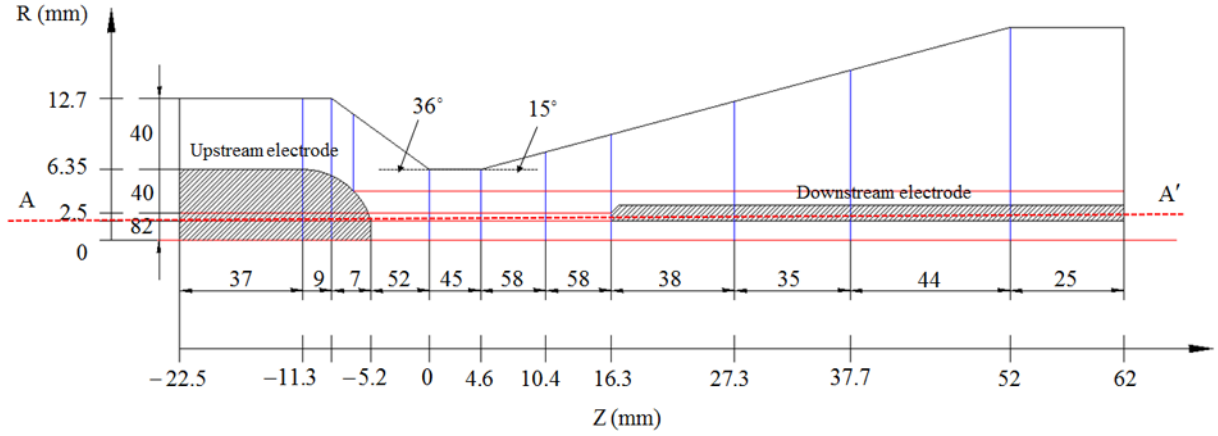

Figure 1. Nozzle geometry and grid system. The computation domain is divided into eleven intervals in the axial direction and four in radial direction. The axial and radial coordinates defining the intervals and the number of cells in each interval are indicated above. Z=0 indicates the axial position of the inlet of flat nozzle throat. There are 162×408 grids. Dense grids are distributed in the arc region with an average grid spacing of 0.1mm in the axial direction.

The current is ramped down towards zero with a fixed value of di/dt, from a DC plateau, I_0, of 1kA. Two values of di/dt, 13 $A\mu s^{-1}$ and 25 $A\mu s^{-1}$, have been investigated. The choice of 1 kA as the plateau ensures quasi-steady state of the arc at this current and the solutions at current zero can be compared with the experimental results. Thus, the peak current of a sinusoidal current does not affect the arc at current zero [18].

For the Prandtl mixing length model, the value of turbulence parameter, c, is adjusted to give the closest agreement with the measured RRRV for P_0 = 21.4 atm and di/dt = 25 $A\mu s^{-1}$ [2]. The value of c = 0.048 was used in Part I [1] where the radial integration of temperature for the computation of r_δ (table 1) extends to the nozzle wall. Since the arc cross section is smaller than that of the nozzle, the temperature tends to local ambient temperature asymptotically. Very fine radial grids need to be used to resolve such asymptotic behaviour, which has little effect on the arc region. In order to save computational time, we terminate the radial integration for r_δ at the position where the temperature difference between two adjacent radial points satisfies the following relation:

$$\left|\frac{T_j - T_{j-1}}{T_j}\right| \le 0.01 \qquad \text{(j=1, 2, 3… n)} \qquad (3)$$

where n is the number of cells in the radial direction. r_δ computed using expression (3) is smaller than that computed with the radial integration extending to the nozzle wall. This results in a smaller mixing length, i.e. turbulence length scale, λ_c (table 1). Thus, c is readjusted to match the computed RRRV with

that measured for P_0 = 21.4 atm and di/dt = 25 Aμs^{-1}. The value of *c* has been found to be 0.057 which has been used throughout this paper.

3.1 Arc behaviour before current zero

It has been found that the qualitative features of the arc behaviour predicted by the five flow models are similar for different values of P_0 and di/dt. Unless otherwise specified, the computed results for P_0 = 21.4 atm and di/dt = 13 Aμs^{-1} will be used to illustrate the typical arc behaviour and the differences between flow models. It has been found that, when the current decreases from 1 kA to 50 A, the computational results of the Prandtl mixing length model and the standard k-epsilon model are very close. Likewise, in this current range, the results of laminar flow, the Chen-Kim and the RNG models are very close to each other. Thus, for the convenience of discussions on the features of computational results, we refer the Prandtl mixing length model and the standard k-epsilon model as Group 1 models and the other three flow models as Group 2.

3.1.1 General arc features

When the current is ramped down, the general features of the arc and its surrounding gas flow are similar to those of the DC arc [1]. In front of the upstream electrode, the wake does not exist at high instantaneous currents, which reappears shortly before current zero (i.e. from the currents just below 50 A). In front of the downstream electrode, there is a compression wave, rather than a bow shock, for currents 400A and above. The bow shock reappears for currents just below 400A.

The choice of 1 kA DC as the plateau of the current ramp ensures a quasi-steady state period of arcing for all chosen five flow models. This ensures the computational results at current zero being independent of the choice of the plateau current. The arc voltage-current (V-I) characteristics (figure 2) in this period show a flat part with a voltage close to the DC voltage for the same current. For the five flow models, quasi-steady state can be maintained down to an instantaneous current of 200 A. Below 200 A the arc voltage deviates greatly from the corresponding DC voltage and an extinction peak is produced for the Group 1 models (figure 2).

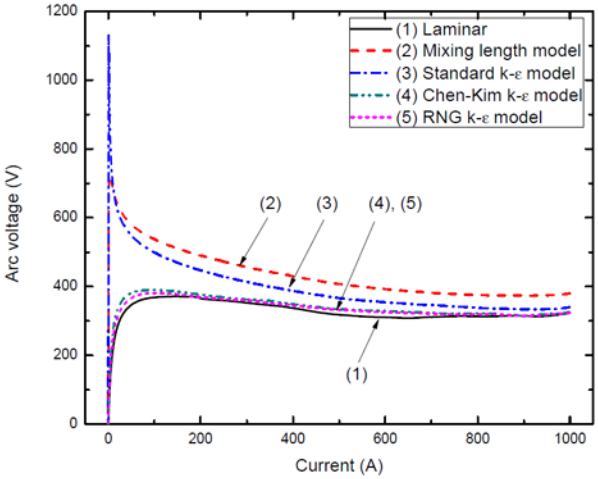

Figure 2. The V-I characteristics for the nozzle arc computed by the five flow models during the current ramp. P_0=21.4 atm and di/dt=13 Aμs^{-1}.

The variations of axis temperature, arc radius (defined by the electrical boundary of the arc

corresponding to the radial position of the 4000 K isotherm), axis pressure and electric field at a few instantaneous currents before current zero are given respectively in figures 3, 4, 5 and 6 for those predicted by the standard k-epsilon model as representative of Group 1 models and those of the Chen-Kim model for Group 2 models. The strength of the compression wave (figure 5) varies with the current but its position does not change when the current decays towards zero. For Group 1 models, the proportion of arc voltage taken up by the arc section downstream of nozzle throat (z = 0 the start of parallel throat section of length 4.6mm in figure 6) increases towards current zero.

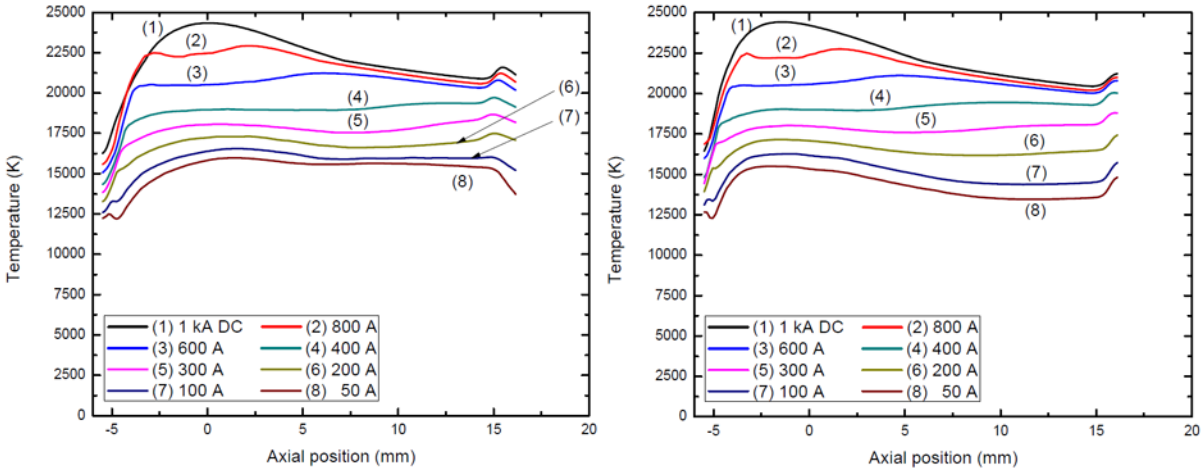

(a) (b)

Figure 3. Variations of axis temperature with axial position at different instantaneous currents before current zero. P_0=21.4 atm and di/dt=13 Aμs^{-1}. (a) Standard k-epsilon model and (b) Chen-Kim model.

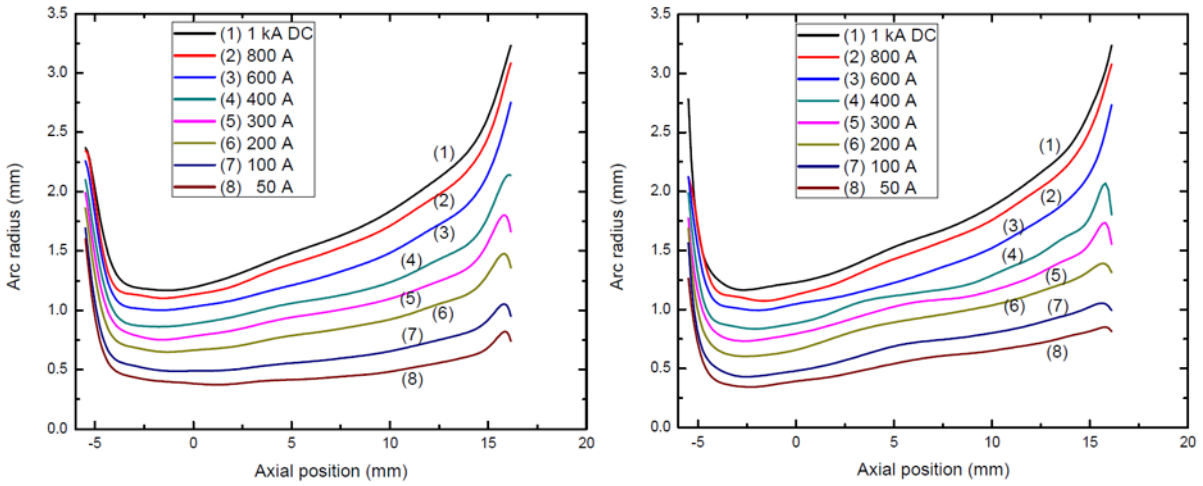

(a) (b)

Figure 4. Variation of arc radius with axial position at different instantaneous currents before current zero. P_0=21.4 atm and di/dt=13 Aμs^{-1}. (a) Standard k-epsilon model and (b) Chen-Kim model.

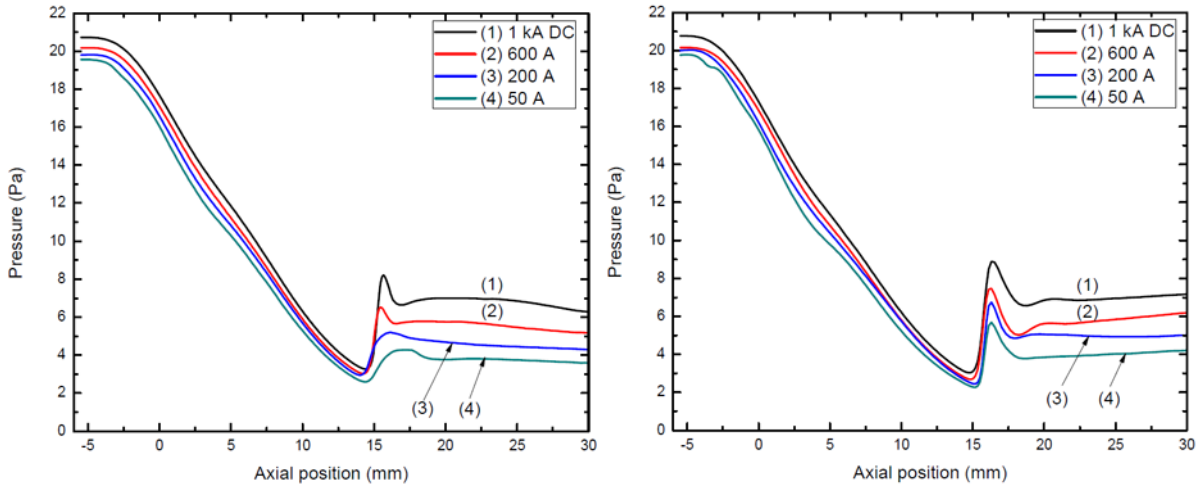

(a) (b)

Figure 5. Variation of axis pressure with axial position at different instantaneous currents before current zero. P_0=21.4 atm and di/dt=13 Aμs^{-1}. (a) Standard k-epsilon model and (b) Chen-Kim model.

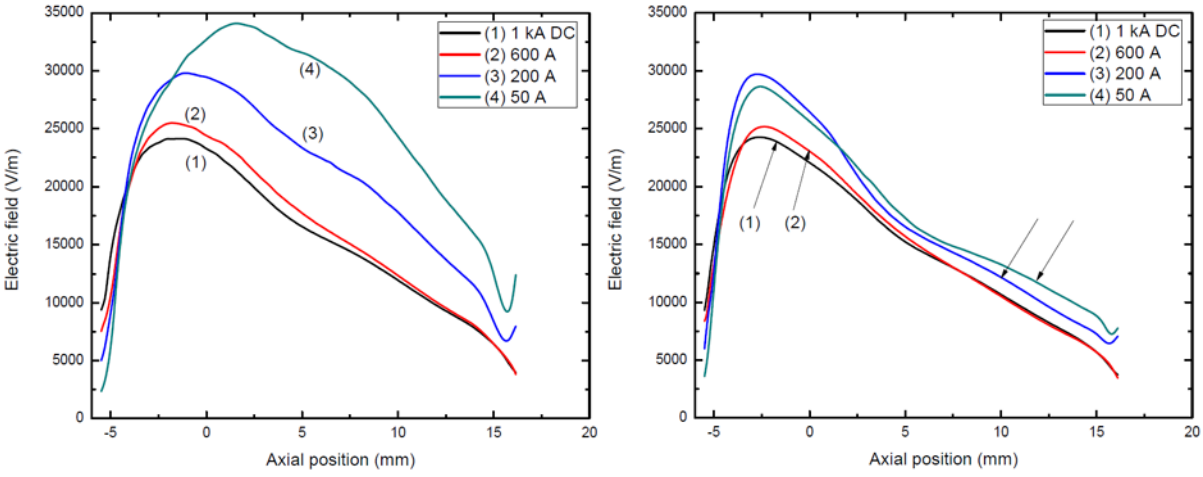

(a) (b)

Figure 6. Variation of electric field with axial position at different instantaneous currents before current zero. P_0=21.4 atm and di/dt=13 Aμs^{-1}. (a) Standard k-epsilon model and (b) Chen-Kim model.

3.1.2 Dominant energy transport process when current decays towards zero

For currents down to 200A, the predicted axis temperature shows little dependence on the flow models (figure 3) although detailed radial temperature profiles (figure 7) differ for different flow models. The radial temperature profiles show a rather flat temperature distribution inside the high temperature arc core (hereafter referred to as the core, the boundary of which is defined as the isotherm of 83% of the axis temperature [16]). Arc voltage is mainly determined by this region where over 80% of the current is carried. Results indicate that, for all flow models, within the arc core radiation transport is dominant, as confirmed by energy balance calculation at 600 A (table 2). Radial thermal conduction (attributed to turbulent energy transport for all the flow models except the laminar flow) at the core boundary for Group 1 models is already an important energy transport mechanism which accounts for over 25% of electrical power input. As 80% of the radiation from this core is absorbed in the radiation re-absorption region between the core boundary and the electrical boundary (defined as the 4000 K isotherm), radial temperature gradient is the steepest for the laminar flow model (figure 7). This is because SF_6 thermal

conductivity (commonly known as the molecular part of thermal conductivity of a turbulent flow) is much smaller than the turbulent counterpart. Energy balance calculation at the electrical boundary for 600 A (table 3) shows that for Group 1 models radial thermal conduction and axial enthalpy transport are dominant. For Group 2 models radiation still accounts for 30% of the power input and axial enthalpy transport is the most important energy removal process. For transient arcs, expansion cooling accounts for less than 7% of power input for Group 1 models and up to 9% for Group 2 models (table 3). Table 2 indicates that the rate of change of energy storage in the arc core accounts for less than 7% of power input. Thus, the core remains approximately in quasi-steady state and the arc voltage is close to that of DC at the same current. However, the rate of change of energy storage up to the electrical boundary (table 3) is already over 10% of the power input. This indicates that the radiation re-absorption region already departs from quasi-steady state at 600A. The effects of the departure from quasi-steady state in this region are not reflected in arc voltage as the current is mainly carried in the core region.

When current decreases towards current zero, thermal conduction becomes the dominant energy loss mechanism and radiation plays a secondary but still a significant role at the core and electrical boundaries for Group 1 models as shown in the energy balance calculation for 50 A (tables 4 and 5). For Group 2 models, the dominant radiation transport together with thermal conduction balance the power input at the core and electrical boundaries. The radial temperature profiles of Group 1 models and those of Group 2 models in the middle section of the parallel throat region of the nozzle (Z = 2.3 mm, figure 7(a)) are virtually the same. However, temperature profiles differ in the downstream (figure 7(b)) for Group 2 models as radial thermal conduction due to turbulence for the Chen-Kim and the RNG models accounted respectively for 39% and 30% of the power input at the electrical core boundary. This is due to the increase in turbulence intensity in the divergent section of the nozzle.

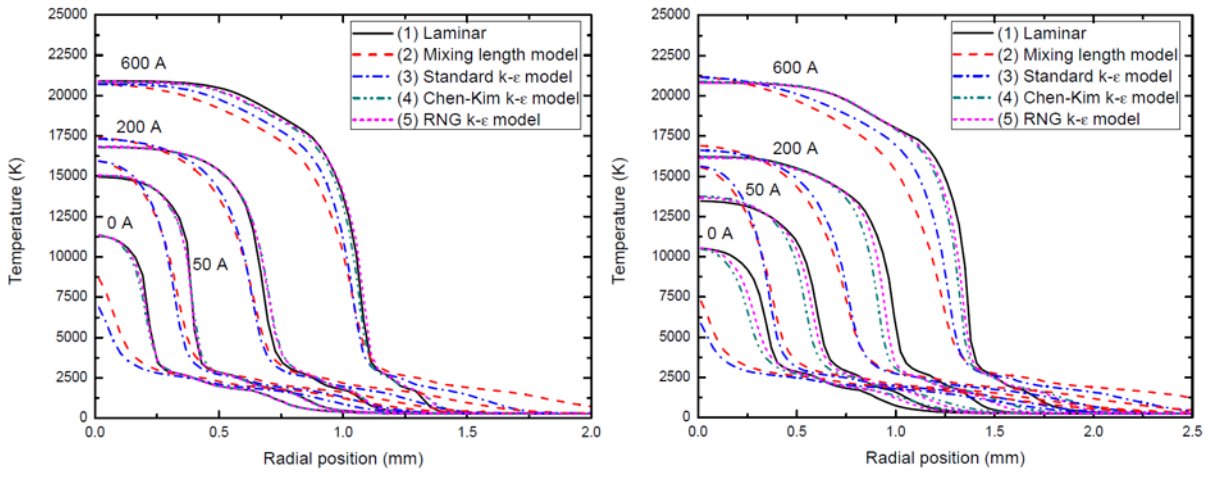

Figure 7. Radial temperature profiles at two axial positions computed by the five flow models at four instantaneous currents before and at current zero (600 A, 200 A, 50 A and current zero). P_0=21.4 atm and di/dt=13 Aμs^{-1}. (a) Z = 2.3 mm (middles section of parallel nozzle throat region) and (b) Z = 7.9 mm (middle section between the exit of throat region and the downstream electrode tip).

Table 2. Percentage of electric power input associated with various energy transport processes for the whole arc length at the core boundary calculated by the five flow models at an instantaneous current of 600 A, P_0=21.4 atm and di/dt=13 Aμs^{-1}. Positive sign means power input and negative sign power loss. This applies to all tables.

Model	Power input (10^5 W)	Radiation loss (%)	Radial thermal conduction (%)	Axial enthalpy transport (%)	Radial enthalpy transport (%)	Expansion cooling (%)	Rate of change of energy storage (%)
(1)	1.49	-69.7	-4.4	-14.1	-7.6	-8.3	6.1
(2)	1.60	-56.7	-37.5	-1.4	-4.3	-4.9	4.3
(3)	1.61	-61.9	-25.6	-7.2	-5.1	-5.7	5.0
(4)	1.59	-68.0	-7.6	-15.5	-6.1	-7.0	5.4
(5)	1.57	-68.3	-6.6	-15.7	-6.1	-7.2	5.5

Method of calculation: $\text{Power input} = \int_{Z1}^{Z2}\left[\int_0^R \sigma E^2 2\pi r dr\right]dz,$

$\text{Radiation loss} = -\int_{Z1}^{Z2}\left[\int_0^R q 2\pi r dr\right]dz,$

$\text{Radial thermal conduction} = \int_{Z1}^{Z2}\left[\int_0^R \frac{1}{r}\frac{\partial}{\partial r}\left(r\frac{k}{c_p}\frac{\partial h}{\partial r}\right)2\pi r dr\right]dz$

$\text{Axial enthalpy transport} = -\int_{Z1}^{Z2}\left[\int_0^R \rho w\frac{\partial h}{\partial z}2\pi r dr\right]dz$

$\text{Radial enthalpy transport} = -\int_{Z1}^{Z2}\left[\int_0^R \rho v\frac{\partial h}{\partial r}2\pi r dr\right]dz$

$\text{Expansion cooling} = \int_{Z1}^{Z2}\left[\int_0^R \frac{dp}{dt}2\pi r dr\right]dz = \int_{Z1}^{Z2}\left[\int_0^R \left(\frac{\partial p}{\partial t} + w\frac{\partial p}{\partial z} + v\frac{\partial p}{\partial r}\right)2\pi r dr\right]dz$

$\text{Rate of change of energy storage} = -\int_{Z1}^{Z2}\left[\int_0^R \rho\frac{\partial h}{\partial t}2\pi r dr\right]dz$

where *R* refers to the radial position of the core boundary or electrical boundary and (Z2-Z1) the arc length.

Key to the models: (1) Laminar flow model, (2) Prandtl mixing length model, (3) Standard k-epsilon model, (4) Chen-Kim k-epsilon model and (5) RNG k-epsilon model.

Table 3. Percentage of electric power input associated with various energy transport processes for the

whole arc length at the electrical boundary calculated by the five flow models at an instantaneous current of 600 A. P_0=21.4 atm and di/dt=13 Aμs^{-1}. Mathematical expressions for power input and power loss and the key to the models are the same as those in table 2.

Model	Power input (10^5 W)	Radiation loss (%)	Radial thermal conduction (%)	Axial enthalpy transport (%)	Radial enthalpy transport (%)	Expansion cooling (%)	Rate of change of Energy storage (%)
(1)	1.84	-31.5	-1.0	-95.0	23.2	-9.0	14.9
(2)	2.34	-15.0	-64.7	-35.6	10.6	-5.6	10.5
(3)	2.11	-23.2	-46.0	-52.4	15.3	-6.3	13.1
(4)	1.96	-31.2	-14.6	-75.1	16.5	-7.7	14.2
(5)	1.94	-31.4	-12.9	-77.6	17.5	-7.9	14.8

Table 4. Percentage of electric power input associated with various energy transport processes for the whole arc length at the core boundary calculated by the five flow models at an instantaneous current of 50 A. P_0=21.4 atm and di/dt=13 Aμs^{-1}. Mathematical expressions for power input and power loss and the key to the models are the same as those in table 2.

Model	Power input (10^4 W)	Radiation loss (%)	Radial thermal conduction (%)	Axial enthalpy transport (%)	Radial enthalpy transport (%)	Expansion cooling (%)	Rate of change of Energy storage (%)
(1)	1.67	-77.6	-20.7	-8.8	-6.1	-13.0	29.8
(2)	2.14	-44.5	-63.9	-0.4	-1.6	-2.4	13.1
(3)	2.24	-47.2	-62.6	0.2	-3.5	-2.9	16.5
(4)	1.80	-74.0	-31.6	-5.8	-7.5	-8.6	29.6
(5)	1.76	-75.9	-28.0	-6.7	-7.1	-10.3	30.5

Table 5. Percentage of electric power input associated with various energy transport processes for the whole arc length at the electrical boundary calculated by the five flow models at an instantaneous current of 50 A. P_0=21.4 atm and di/dt=13 Aμs^{-1}. Mathematical expressions for power input and power loss and the key to the models are the same as those in table 2.

Model	Power input (10^4 W)	Radiation loss (%)	Radial thermal conduction (%)	Axial enthalpy transport (%)	Radial enthalpy transport (%)	Expansion cooling (%)	Rate of change of Energy storage (%)
(1)	1.80	-64.7	-3.2	-102.0	-21.0	-16.8	111.0
(2)	2.99	-23.8	-93.9	-15.2	-11.1	-4.5	50.2
(3)	2.83	-30.5	-88.7	-12.0	-20.5	-4.6	57.8
(4)	1.98	-59.3	-38.7	-55.0	-27.2	-11.3	93.7
(5)	1.90	-62.4	-30.0	-63.5	-27.8	-13.5	99.9

Table 6. Electric power input together with various energy transport processes for the whole arc length at the electrical boundary calculated by the five flow models at current zero. P_0=21.4 atm and di/dt=13 $A\mu s^{-1}$. Mathematical expressions for power input and power loss and the key to the models are the same as those in table 2.

Model	Power input (W)	Radiation loss (W)	Radial thermal conduction (W)	Axial enthalpy transport (W)	Radial enthalpy transport (W)	Expansion cooling (W)	Rate of change of Energy storage (W)
(1)	0.0	-1.03×10^3	-3.65×10^2	-7.71×10^3	-5.39×10^3	-1.16×10^3	1.57×10^4
(2)	0.0	-1.79×10^2	-5.66×10^3	-6.23×10^2	-4.11×10^3	-1.79×10^2	1.08×10^4
(3)	0.0	-3.52×10^2	-5.43×10^3	-4.30×10^2	-4.99×10^3	-2.22×10^2	1.16×10^4
(4)	0.0	-8.71×10^2	-3.47×10^3	-3.16×10^3	-6.24×10^3	-6.84×10^2	1.44×10^4
(5)	0.0	-9.51×10^2	-2.94×10^3	-3.87×10^3	-6.11×10^3	-8.29×10^2	1.47×10^4

3.1.3 Arc conditions in the vicinity of current zero

Axis temperature and arc radius at current zero determine the RRRV which a nozzle interrupter can withstand. When radiation is the dominant energy transport process within the core of the arc, axis temperature is not sensitive to the flow models (figure 3) although arc radii computed by Group 1 models are smaller than those of Group 2 models (figure 4) for currents down to 200 A. For currents below 200 A, energy balance calculation at electrical boundary shows that radial thermal conduction gradually becomes dominant. At 50 A (table 5), thermal conduction almost accounts for the entire electric power input for Group 1 models. For Group 2 models, radiation and axial enthalpy transport are of equal importance and the required radial enthalpy transport determines the radial extent of the arc. Thus, when current decays towards zero, arc radial temperature profile exhibits the features of a thermal conduction dominated arc for Group 1 models, which is rather constricted (figure 7) with a much smaller arc radius than those of Group 2 models (figure 4). When the current approaches zero, with a smaller arc radius and enhanced thermal diffusivity due to turbulence, the rate of arc temperature decay is accelerated as shown in figure 8 immediately before current zero especially for the standard k-epsilon model. A radial inflow is generated for Group 1 models which supplies gas to the arc core as required by the rapid temperature decay. This radial inflow of cold gas in turn accelerates the temperature decay and the fast reduction in arc size. An extinction peak is produced (figure 2) for Group 1 models. The role of turbulent transport of energy becomes increasingly important towards current zero. Since turbulence intensity increases along the arc, a large proportion of the arc voltage is taken up by the arc section downstream of nozzle throat for Group 1 models (figure 6(a)), while for Group 2 models voltage is mainly taken up by arc section upstream of nozzle throat (figure 6(b)).

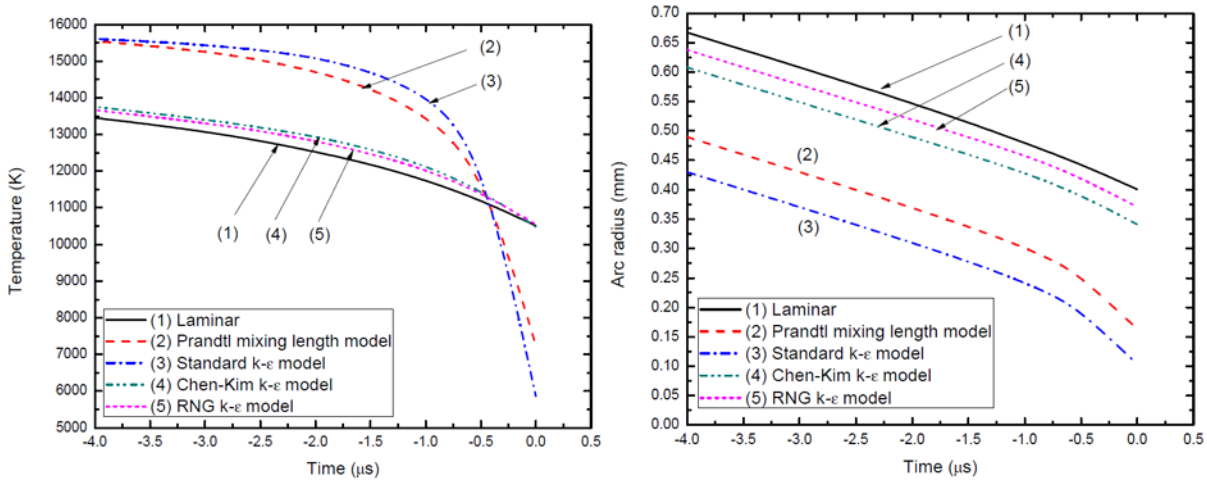

(a) (b)

Figure 8. Axis temperature and arc radius at Z=7.9mm as a function of time from the instant of 50 A down to zero for the five flow models. P_0=21.4 atm and di/dt=13 Aμs^{-1}. (a) Axis temperature and (b) arc radius.

Arc axis temperature and arc radius differ (figure 9) greatly with flow models at current zero due to widely different rates of temperature decay and the differing dominant energy transport processes. Because of the dominance of radiation transport for Group 2 models (table 4), axis temperature is almost the same for the three flow models in this group (figure 9(a)). The increases in axis temperature and arc radius near the downstream electrode are due to the bow shock as shown in Part I [1]. Shock position and structure differ depending on the flow models (figures 5 and 9). This region is approximately 2 mm in thickness. The voltage drop in this region (figure 6(a)) is negligible in comparison with the total arc voltage. Therefore, the uncertainty with regard to the bow shock will not affect RRRV.

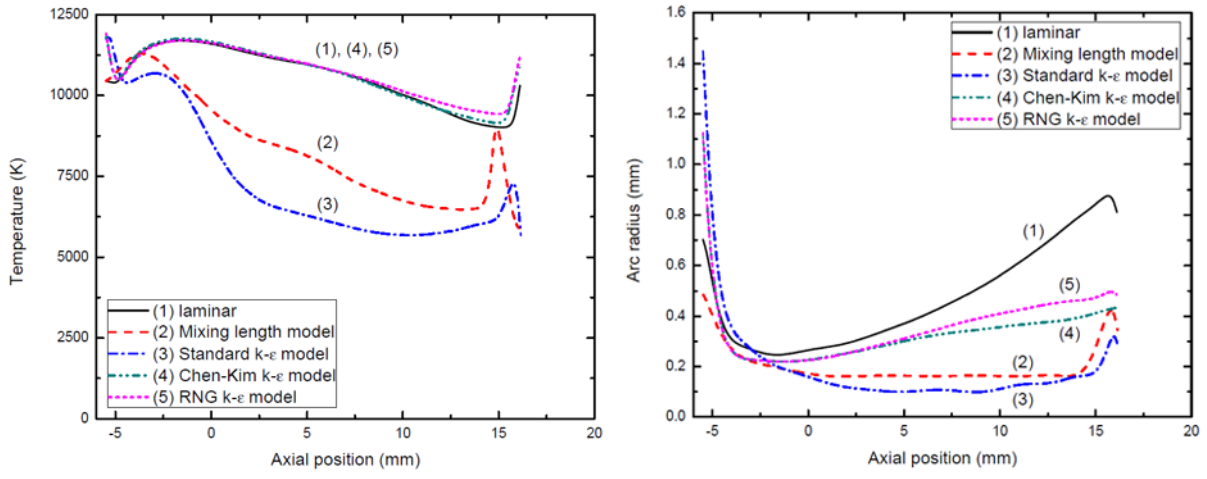

(a) (b)

Figure 9. Variations of axis temperature and arc radius with axial position at current zero. (a) Axis temperature and (b) arc radius.

3.2 Dependence of arc conditions at current zero on turbulence cooling

It has been shown in the previous section that axis temperature and arc radius at current zero are strongly dependent upon the flow models. Such dependence can be attributed to the dominance of turbulence cooling especially in the 2 μs before current zero for the Group 1 models. The level of turbulence cooling is reflected in eddy viscosity, μ_t, which is directly linked to turbulent thermal conductivity though turbulent Prandtl number. It is therefore of interest to compare the eddy viscosity at current zero computed by the four turbulence models. Since turbulence effects are more pronounced in the downstream of nozzle throat, we choose an axial station which is in the middle between the exit of the throat region and the tip of downstream electrode (Z=7.9 mm) to illustrate the dependence of μ_t on turbulence models at current zero (figure 10). Of the four turbulence models the standard k-epsilon predicts the highest eddy viscosity, which is then followed by that of Prandtl mixing length model. The strongest turbulence cooling is therefore predicted by the standard k-epsilon model, which results in the fastest rate of temperature decay before current zero (figure 8(a)). As a result, the standard k-epsilon model grossly over predicts RRRV in comparison with experimental results (Section 3.4).

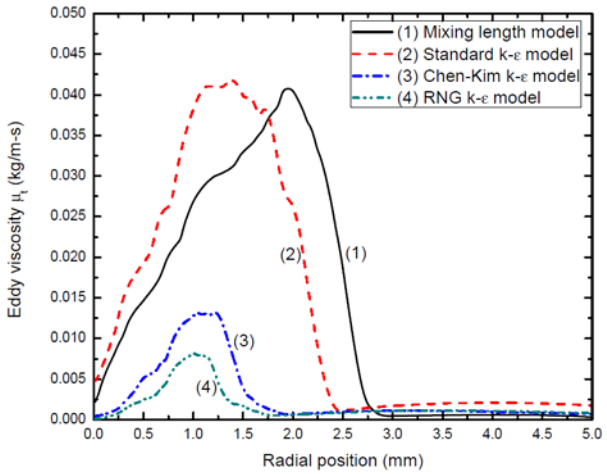

Figure 10. Radial profiles of the eddy viscosity at Z = 7.9mm computed by different turbulence models at current zero. P_0=21.4 atm and di/dt=13 Aμs^{-1}.

3.3 Arc behaviour after current zero and RRRV

A linearly increasing voltage at a given rate of rise (dV/dt, known as the rate of rise of recovery voltage) is used after current zero to investigate the thermal interruption capability of the nozzle interrupter. The value of dV/dt, at which the arc will just be extinguished, is commonly known as the RRRV. This will be found computationally by applying all the five flow models. The qualitative features of the arc behaviour after current zero are similar when for different values of P_0 and di/dt. Unless otherwise specified, results are presented for P_0=21.4 atm and di/dt=13 Aμs^{-1}.

Typical results of post-arc current predicted by the five flow models are given in figure 11. The peak of post arc current in the vicinity of RRRV does not exceed 0.1 A with a duration of no longer than 0.5 μs for Group 1 models (figure 11(a)) but for Group 2 models the corresponding values are an order of magnitude higher than those of Group 1 models (figure 11(b)). Computed axis temperature and electric field distributions at different instants after current zero are given in figure 12 for the Prandtl mixing length model. Results obtained by the other flow models are not given, since they are qualitatively similar to those computed by the Prandtl mixing length model.

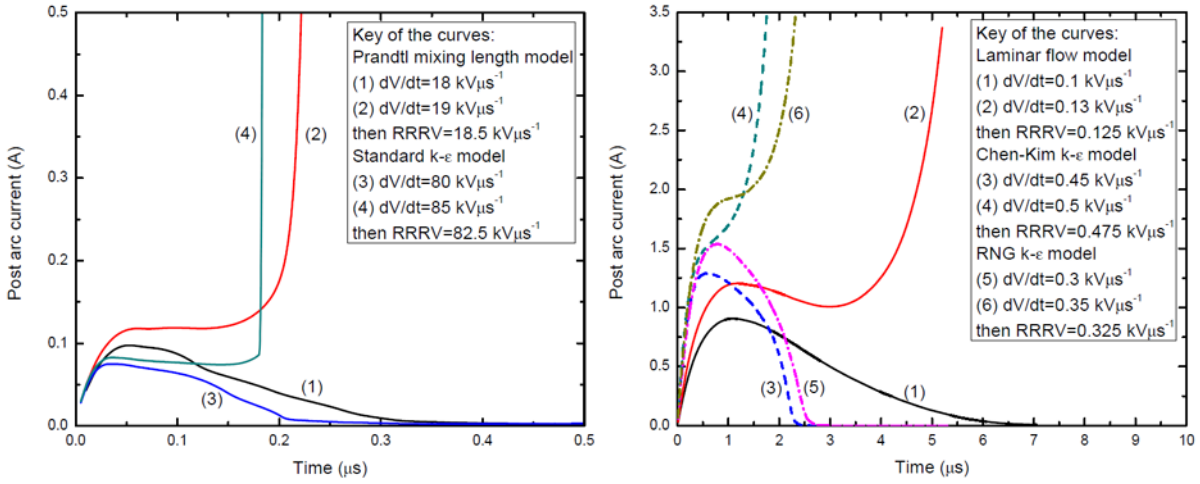

(a) (b)

Figure 11. Post-arc current predicted by the five flow models, for P_0=21.4 and di/dt=13 Aμs^{-1}. (a) Group 1 models and (b) Group 2 models.

For the Prandtl mixing length model, when the arc is thermally extinguished, arc axis temperature decays within 0.5 μs to below 4000 K after current zero (figure 12(a)). The rapidly rising recovery voltage is mainly taken up by an arc section of 9mm long downstream of the parallel throat region (5mm< Z<14mm, figure 12(b)). This section (commonly known as the critical section) plays the decisive role for arc extinction. Turbulent thermal conduction is responsible for the rapid cooling of the arc. The standard k-epsilon model predicts similar arc behaviour after current zero. However, this model predicts a longer critical section (2.5 mm<Z<14 mm) than that predicted by the Prandtl mixing length model, and a more rapid temperature decay rate. Axis temperature falls below 4000 K within only 0.25 μs. This is due to stronger turbulence cooling effects predicted by this model from the instants shortly before current zero as previously discussed. The RRRV computed by the standard k-epsilon model is therefore significantly higher than that obtained by the Prandtl mixing length model as shown in figure 11(a).

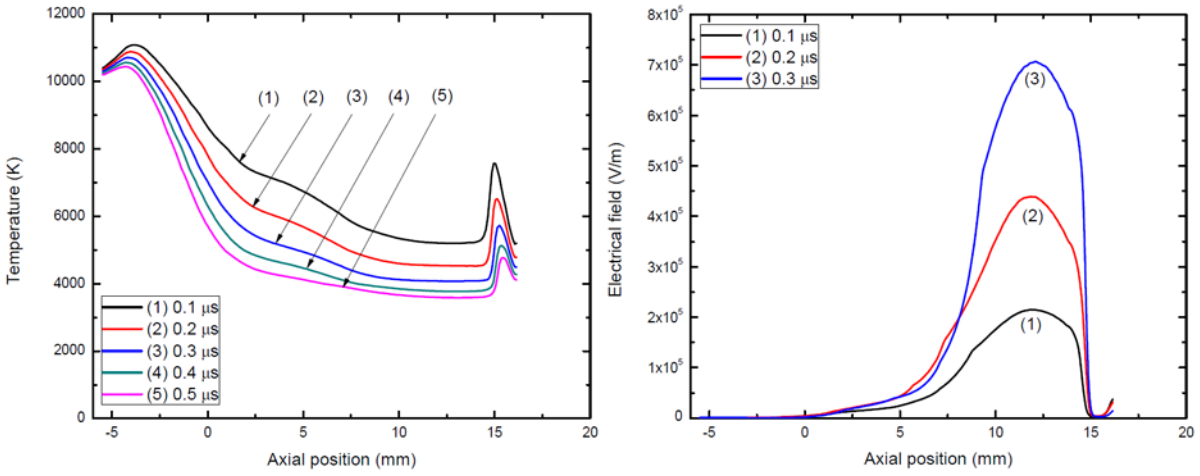

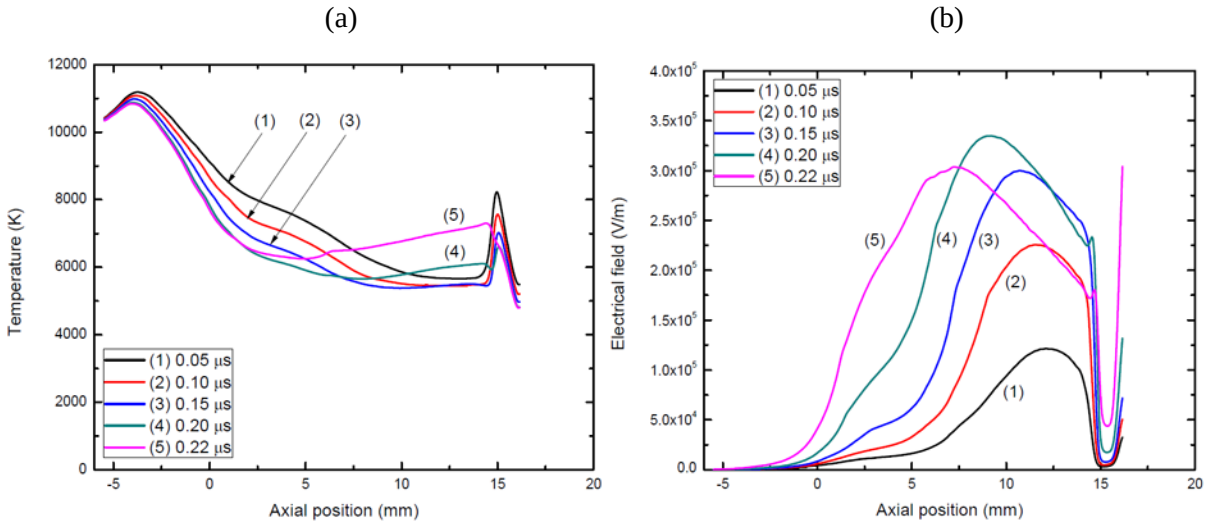

Figure 12. Axis temperature and electrical field distributions at various instants after current zero for the Prandtl mixng length model. (a) Axis temperature distribution and (b) electrical field distribution for dV/dt = 18 kVμs^{-1} (thermal clearance); (c) Axis temperature distribution and (d) electrical field distribution for dV/dt = 19 kVμs^{-1} (thermal reignition).

If dV/dt exceeds RRRV, temperature in the critical region still reduces immediately after current zero due to thermal inertia but this temperature decay is soon arrested (figure 12(c)) as the power input is pumped into a very thin core of the critical section. When the axis temperature starts rising, the temperature in the surrounding region still decreases. Thus, the rapid increase in axis temperature (figure 12(c)) does not result in collapse of the voltage taken up by this section (figure 12(d)). When the decay of temperature away from the axis has been arrested, the rate of rise of current is extremely rapid for a given the dV/dt above RRRV (figure 11(a)). Thus, the critical section is also responsible for thermal reignition.

It is noted that electric field has a high value right in front of the downstream electrode (figure 12(d)). Examination of the results shows that the axis temperature and arc radius are both reduced immediately in front of the downstream electrode, which results in a sudden increase of electrical field in this region. This is because the deceleration of the flow into the shock and as well as flow reversal gives rise to large values of the local velocity gradients (i.e. $\partial w/\partial r$ and $\partial v/\partial z$) right in front of the downstream electrode, which has the effects of increasing the μ_t and thus the turbulence level. The resulting strong turbulence cooling effect results in low temperature and small arc radius, and thus sudden increase of electric field, in front of the downstream electrode. As shown in [1, 19] the structure of the shock depends on the flow model. There are no direct experimental results revealing shock structure. No firm conclusions can therefore be drawn about the influence of the bow shock in front of the downstream electrode. However, the effects of this region are negligible in term of its contribution to total arc voltage.

When dV/dt is at RRRV or below, Chen-Kim and the RNG models both predict a shorter critical section of the arc (from 8 mm to 14 mm) and a much slower cooling rate than those predicted by Group 1 models because of much reduced turbulence cooling effects. The laminar flow model predicts the lowest RRRV

which is an order of magnitude below that of the Prandtl mixing length model (figure 11).

3.4 Comparison with experiments

The computed RRRV as a function of P_0 at di/dt=13 and 25 Aμs^{-1} are plotted in figure 13 together with the experimental results given in [2] for comparison. The dependence of RRRV on P_0 at a given di/dt computed by the five flow models are listed in table **7**.

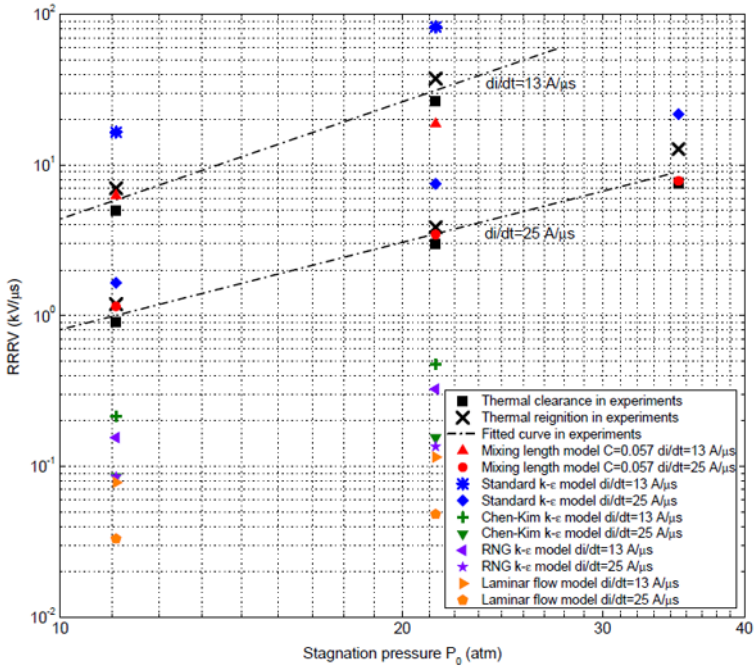

Figure 13. Comparison of measured RRRV and predicted RRRV computed by the five flow models.

Table 7. The dependence of RRRV on P_0 at a given di/dt computed by the four turbulence models.

	di/dt=13 Aμs^{-1}		di/dt=25 Aμs^{-1}	
	Predictions	Experiments	Predictions	Experiments
Laminar flow model	RRRV $\propto P_0^{0.6}$	RRRV $\propto P_0^{y}$ 2.05 < y < 3.11	RRRV $\propto P_0^{0.58}$	RRRV $\propto P_0^{y}$ 1.63 < y < 2.33
Prandtl mixing length model	RRRV $\propto P_0^{1.73}$		RRRV $\propto P_0^{1.69}$	
Standard k-epsilon model	RRRV $\propto P_0^{2.5}$		RRRV $\propto P_0^{2.26}$	
Chen-Kim k-epsilon model	RRRV $\propto P_0^{1.2}$		RRRV $\propto P_0^{0.93}$	
RNG k-epsilon model	RRRV $\propto P_0^{1.15}$		RRRV $\propto P_0^{0.66}$	

It is well known that there is large scatter in experimentally measured RRRV due to shot to shot variation. In addition to shot to shot variation, the experimental results of [2] also show a range of uncertainty of experimental value of RRRV, which is equal to the differences between experimentally measured dV/dt for arc extinction and that for arc reignition (figure 13). The average value of uncertainty for the experimental results (figure 13) in percentage of experimentally measured dV/dt for arc extinction is 40%. Because of this experimental uncertainty, the exponent of the dependence of the RRRV on stagnation pressure (i.e. y in $\text{RRRV} \propto P_0^y$) ranges from 2.05 to 3.11 for di/dt = 13 $A\mu s^{-1}$ and from 1.63 to 2.33 for di/dt= 25 $A\mu s^{-1}$ (table 7). The same value of y must be applicable to both di/dt to avoid the intersection of the two straight lines in figure 13. Intersection of the straight lines implies that for pressures smaller than that of the intersection point, RRRV would be higher for a larger value of di/dt, which is not physical. The two ranges of y, derived for di/dt = 13 $A\mu s^{-1}$ and 25 $A\mu s^{-1}$, overlap for $2.05 < y < 2.33$. It is therefore reasonable to choose $y = 2.1$ for the pressured dependence of RRRV for both values of di/dt investigated. It should be noted that the experimental results of Plessel [19] show $y = 1.6$, which agrees with the prediction of Hermann et al [20] and Hermann and Ragaller [21].

The RRRV predicted by the Prandtl mixing length model with the chosen value of turbulence parameter shows excellent agreement with experiments at di/dt=25 $A\mu s^{-1}$. For di/dt= 13 $A\mu s^{-1}$ and P_0 = 21.4 atm, the predicted RRRV is lower than the experimental value of dV/dt for arc extinction. However, this is within the range of experimental uncertainty. The computed average value of the exponent of the pressure dependence of RRRV is 1.71 which is considered satisfactory in view of 40% of uncertainty in experimentally measured RRRV. The Prandtl mixing length model can predict thermal interruption capability of the nozzle interrupter under investigation within experimental error.

The standard k-epsilon model grossly over-predicts the values of RRRV. In comparison with the Prandtl mixing length model, this model predicts a much stronger dependence of RRRV on P_0 at two values of di/dt investigated (figure 13).

The laminar flow model predicts the lowest values of RRRV, which is on average two orders of magnitudes lower than the measured dV/dt at which the arc is extinguished. The computed RRRV is approximately proportional to the square root of P_0, which is consistent with the investigation of [22] for laminar SF_6 arc.

The Chen-Kim and the RNG models give similar predictions of RRRV, both of which grossly under-estimate RRRV for all cases investigated. Compared with experiments reported in [2], the RRRV computed by the Chen-Kim model and the RNG model also shows much weaker dependence on P_0 at both values of di/dt (13 and 25 $A\mu s^{-1}$), which is only slightly stronger than the dependence predicted by the laminar flow model.

4 The dependence of RRRV on P_0

It is well known that, for a given nozzle, the DC arc voltage is proportional to the square root of P_0 [1]. However, the experimentally measured RRRV and those predicted by the Prandtl mixing length model and the standard k-epsilon model are approximately proportional to the square of P_0. Detailed

examination of computational results obtained by the two flow models for the two values of P_0 investigated indicates that such pressure dependence of RRRV is due to the complex dynamics of nonlinear physical processes embedded in the arc conservation equations together with those describing turbulence transport. Temperature and velocity fields, electric field and turbulence effects are closely coupled through nonlinear transport properties, radiation transport and eddy viscosity. The state of the arc at current zero depends on the arcing history after the breakdown of quasi-steady state. It is, therefore, difficult to identify a particular physical process which depends explicitly on pressure. Investigation is undertaken to see if arc resistance at current zero is influenced by P_0. Arc resistance at current zero is determined by arc temperature and the plasma volume with a temperature above 4000 K. SF_6 is considered as an insulator below 4000 K at which electrical conductivity is negligibly small. We examine the computational results of the Group 1 models for di/dt=13 $A\mu s^{-1}$ at P_0=11.2 atm and 21.4 atm to see how arc resistance evolves before current zero.

The cross section of SF_6 DC arc is inversely proportional to the square root of P_0 [1]. Thus, for a given di/dt, a nozzle arc at a higher value of P_0 would remain in quasi-steady state longer than an arc at a lower value of P_0 with same di/dt. When arc is in quasi-steady state, arc voltage is proportional to square root of P_0 (flat part of the curves in figure 14(a)). Since the arc with P_0 = 11.2 atm breaks from quasi-steady state first (hence entering into current zero period), its instantaneous voltage is smaller than the corresponding DC voltage at the same current. Thus, the voltage ratio of the two arcs at P_0 = 21.4atm and 11.2 atm will be higher than the square root of the stagnation pressure ratio (i.e. 21.4 atm/11.2 atm = 1.91) since the arc at a higher P_0 is still in quasi-steady state. However, such effects are not very pronounced. For example, computational results of arc voltage ratio at an instantaneous 5 A for the two stagnation pressures show a 10% increase above the square root of pressure ratio (figure 14(b)). As previously noted, the rate of axis temperature decay increases rapidly about 1 μs before current zero (figures 8 and 15(a)). Temperature decays faster for an arc with a higher stagnation pressure (figure 15(a)). Such a fast decay of arc temperature is due to turbulence enhanced thermal conduction and a strong radial inflow of cold gas to supply the gas required by the increase in gas density due to rapid temperature decay. The rate of increase of arc resistance (figure 15(b)) is even more rapid than the temperature as the arc radius reduces at a fast rate (figure 4). At di/dt=13 $A\mu s^{-1}$, arc resistance ratio at current zero is approximately equal to the power of 1.95 of the stagnation pressure ratio for the Prandtl mixing length model and to the power of 2.71 for the standard k-epsilon model (figure 15(b)). These ratios are close to the pressure dependence of RRRV predicted by these two flow models as well as that indicated by measurements of [2]. Since arc resistance at current zero determines the post arc current, pressure scaling of RRRV according to resistance pressure ratio at current zero appears reasonable. It is not possible to derive a simple analytical expression for the dependence of RRRV on pressure from arc governing equations as all processes are strongly coupled and their effects are accumulated during the current zero period.

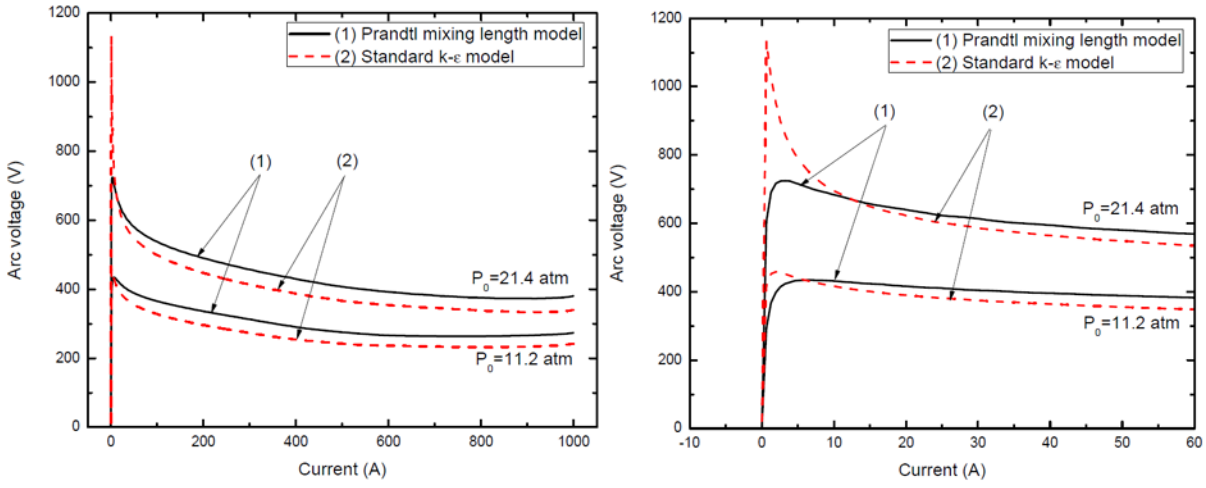

(a) (b)

Figure 14. The voltage-current (V-I) characteristics for the nozzle arcs computed by the Prandtl mixing length model and the standard k-epsilon model corresponding to the current ramp. P_0= 11.2 atm and 21.4 atm, and, di/dt=13 Aμs−1. (a) V-I characteristics and (b) enlarged V-I characteristics in the last 5 μs before current zero.

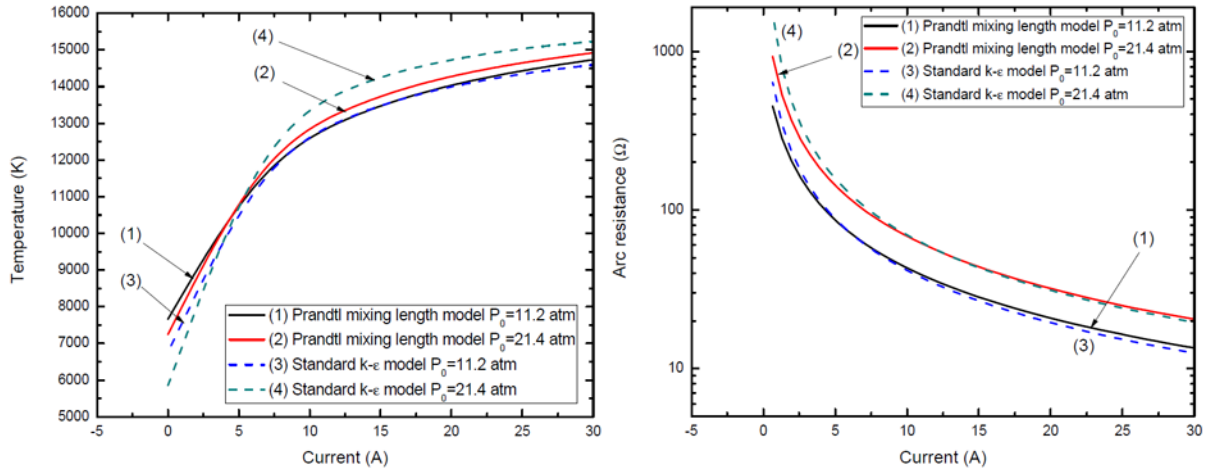

(a) (b)

Figure 15. Variation of axis temperature and arc resistance as a function of current (instant) shortly before current zero for Z=7.9 mm. Results are obtained by the Prandtl mixing length model and the standard k-epsilon model. P_0= 11.2 atm and 21.4 atm, and, di/dt=13 $A\mu s^{-1}$. (a) axis temperature and (b) arc resistance.

5 Relative merits of turbulence models

Of the four turbulence models investigated, the Prandtl mixing length model is the simplest but the turbulence parameter needs to be tuned to give the best agreement with a single set of experimental results. If nozzle geometry is changed, this process needs to be repeated.

As regards the predicted RRRV, the Prandtl mixing length model can generally give satisfactory predictions for a range of P_0 and di/dt with the chosen turbulence parameter for a given nozzle geometry. It is obvious that the standard k-epsilon model overestimates RRRV while its two variants (the Chen-Kim model and the RNG model) underestimate for the same reason given in Part I [1].

It is possible that one of the recommended values of the turbulence parameters in the standard k-epsilon model and its two variants (the Chen-Kim model and the RNG model) could be adjusted to achieve agreement with test results. If such adjustment is successful the Prandtl mixing length model is still preferred on consideration of computational cost and simplicity.

6 Conclusions

The aerodynamic and electrical behaviour of the transient SF_6 nozzle arc has been numerically investigated using the five flow models employed in Part I [1]; the laminar flow model, the Prandtl mixing length model, the standard k-epsilon model, the Chen-Kim model and the RNG model.

A detailed comparative study of different flow models has been conducted for P_0=21.4 atm and di/dt=13 $A\mu s^{-1}$. For currents down to 200 A, radiation loss is the dominant energy transport process within the high temperature arc core where 80% of the current is conducted. Thermal conduction is not significant during this period, and thus the predicted arc behaviour is not sensitive to flow models. It is also found that the arc at the currents of 200 A and above can remain approximately in quasi-steady state. When the current decreases towards zero, thermal conduction becomes significant and arc behaviour predicted by different flow models differs widely. A detailed analysis of the physical mechanisms encompassed in each flow model has been given, with the emphasis on the adequacy of a particular model in describing the rapidly varying arc around current zero.

RRRV has been found computationally using the five flow models, which are compared with the measurements of Benenson et al [2]. It has been shown that the Prandtl mixing length model can give satisfactory predictions of the RRRV with turbulence parameter adjusted to fit one test result of RRRV. Relative merits of the four turbulence models are established by a comparison between the predicted RRRV and those measured.

The pressure dependence of the measured RRRV and those predicted by the Prandtl mixing length model and the standard k-epsilon model are close to the square of stagnation pressure, P_0, rather than to the square root of P_0 for the DC arc. Such strong pressure dependence is the nonlinear behaviour of the arc, which cannot be attributed to a particular gas property or a physical process explicitly dependent upon pressure. This results in the rapid decay of arc temperature and the shrinkage of the electrically conducting core 1 μs before current zero under the combined influence of turbulent enhanced thermal conduction and the radial inflow of cold gas. It has been found that arc resistance at current zero increases with the square of P_0. It is suggested that RRRV is strongly correlated to the arc resistance at current zero, hence the pressure dependence of RRRV.

References

[1] Zhang Q, Yan J D and Fang M T C 2014 The modelling of an SF_6 arc in a supersonic nozzle: I. Cold flow features and dc arc characteristics *J. Phys. D: Appl. Phys.* **47** 215201

[2] Benenson D M, Frind G, Kinsinger R E, Nagamatsu H T, Noeske H O and Sheer, Jr R E 1980 Fundamental investigation of arc interruption in gas flows *Final report General Electric Co.* (Schenectady, NY) Project 246-2

[3] Seeger M, Galletti B, Bini R, Dousset V, Iordanidis A, Over D, Mahdizadeh N, Schwinne M, Stoller P and Votteler T 2014 Some aspects of current interruption physics in high voltage circuit breakers *Contrib. Plasma Phys.* **54** 225-34
[4] Leseberg D and Pietsch G 1982 Optical investigation on SF_6 switching arc inside a glass nozzle *Proc. 7th Int. Conf. on Gas Discharges and Their Applications (London)* pp 9-12
[5] Kobayashi A, Yanabu S, Yamashita S and Ozaki Y 1980 Experimental investigation on arc phenomena ins SF6 puffer circuit breakers *IEEE Trans. Plasma. Sci.* **PS-8** 339-43
[6] Bini R, Basse N T and Seeger M 2011 Arc induced turbulent mixing in an SF_6 circuit breaker model *J. Phys. D: Appl. Phys.* **44** 025203
[7] Wilcox D C 2006 Turbulence Modeling for CFD (La Cañada, CA: DCW Industries)
[8] Fang M T C, Zhuang Q and Guo X J 1994 Current zero behaviour of an SF_6 gas-blast arc Part II: turbulent flow *J. Phys. D: Appl. Phys.* **27** 74-83
[9] Yan J D, Nuttall K I and Fang M T C J 1999 A comparative study of turbulence models for SF6 arcs in a supersonic nozzle *J. Phys. D: Appl. Phys.* **32** 1401-6
[10] Song K D, Lee B Y and Park KY 2003 Analysis of thermal recovery for SF_6 gas blast arc within a Laval nozzle *Japan. J. Appl. Phys*. **42** 7073–9
[11] Zhang J L, Yan J D and Fang M T C 2000 Investigation of the effects of pressure ratios on arc behaviour in a supersonic nozzle *IEEE Trans. Plasma Sci.* **28** 1725–34
[12] Song K D, Lee B Y and Park K Y 2004 Calculation of the post-arc current in a supersonic nozzle by using the K-epsilon model *Journal of Korean Physical Society.* **45** 1537-43
[13] Zhang Q, Yan J D and M T C Fang 2012 Modelling of turbulent arc burning in a supersonic nozzle *Proc. Int. Conf. on Gas Discharges and Their Applications (Beijing)* vol 38 pp 202–5
[14] Seeger M , Schwinne M , Bini R, Mahdizadeh N and Votteler T 2012 Dielectric recovery in a high-voltage circuit breaker in SF_6 *J. Phys. D: Appl. Phys.* **45** 395204
[15] Frost L S and Liebermann R W 1971 Composition and transport properties of SF_6 and their use in a simplified enthalpy flow arc model *Proc. IEEE.* **59** 474-85
[16] Zhang J F, Fang M T C and Newland D B 1987 Theoretical investigation of a 2 kA arc in a supersonic nozzle *J. Phys. D: Appl. Phys.* **20** 368-79
[17] PHOENICS is the name of a commercial CFD package supplied by CHAM which is based at Bakery House, 40 High Street, Wimbledon Village, London, SW19 5AU, UK.
[18] Frind G, Kinsinger R E, Miller R D, Nagamatsu H T and Noeske H O 1977, Fundamental investigation of arc interruption in gas flows *Final report General Electric Co.* (Schenectady, NY) Project 246-1
[19] Plessl A 1982 The influence of pressure profiles on gas blast arc interruption *Proc. Int. Conf. on Gas Discharges and Their Applications (London)* pp 32–5
[20] Hermann W, Kogelschatz U, Niemyer L, Ragaller K and Schade E 1976 Investigation on the phenomena around current zero in HV gas blast circuit breakers IEEE Trans. Power Appr. Syst. PAS-95 1165-76
[21] Hermann W and Ragaller K 1977 Theoretical description of the current interruption of HV gas-blast breakers *IEEE Trans. Power App. Syst.* **PAS-96** 1546-55
[22] Fang M T C and Zhuang Q 1992 Current-zero behaviour of an SF_6 gas-blast arc. Part I: laminar flow *J. Phys. D: Appl. Phys.* **25** 1197-204